RESEARCH ARTICLE

Volumetric three-component velocimetry measurements of the turbulent flow around a Rushton turbine

Kendra V. Sharp · David Hill · Daniel Troolin · Geoffrey Walters · Wing Lai

Abstract Volumetric three-component velocimetry measurements have been taken of the flow field near a Rushton turbine in a stirred tank reactor. This particular flow field is highly unsteady and three-dimensional, and is characterized by a strong radial jet, large tank-scale ring vortices, and small-scale blade tip vortices. The experimental technique uses a single camera head with three apertures to obtain approximately 15,000 three-dimensional vectors in a cubic volume. These velocity data offer the most comprehensive view to date of this flow field, especially since they are acquired at three Reynolds numbers (15,000, 107,000, and 137,000). Mean velocity fields and turbulent kinetic energy quantities are calculated. The volumetric nature of the data enables tip vortex identification, vortex trajectory analysis, and calculation of vortex strength. Three identification methods for the vortices are compared based on: the calculation of circumferential vorticity; the calculation of local pressure minima via an eigenvalue approach; and the calculation of swirling strength again via an eigenvalue approach. The use of two-dimensional data and three-dimensional data is compared for vortex identification; a 'swirl strength' criterion is less sensitive to completeness of the velocity gradient tensor and overall provides clearer identification of the tip vortices. The principal components of the strain rate tensor are also calculated for one Reynolds number case as these measures of stretching and compression have recently been associated with tip vortex characterization. Vortex trajectories and strength compare favorably with those in the literature. No clear dependence of trajectory on Reynolds number is deduced. The visualization of tip vortices up to 140° past blade passage in the highest Reynolds number case is notable and has not previously been shown.

K. V. Sharp (✉)
Department of Mechanical and Nuclear Engineering,
Penn State University, 157 Hammond Building,
University Park, PA 16802, USA
e-mail: ksharp@mne.psu.edu

D. Hill · G. Walters
Department of Civil and Environmental Engineering,
Penn State University, 212 Sackett Building,
University Park, PA 16802, USA
e-mail: dfh4@psu.edu

D. Troolin · W. Lai
TSI Incorporated, 500 Cardigan Road, Shoreview, MN, USA

1 Introduction

1.1 Towards three-dimensional image-based velocimetry

Particle imaging methods have developed rapidly over the past two decades (Adrian [2005]). This development has been assisted by increasing experimental capabilities and has been motivated by the goal of increasing the dimensionality and resolution of the obtained data. The ultimate goal is to obtain instantaneous volumetric measurements of the complete (three-components) velocity vector with very high temporal and spatial resolutions. Highly-resolved three-dimensional data will allow for the precise evaluation of velocity and acceleration fields and of gradient-based variables such as vorticity and dissipation.

Classic PIV (Adrian [1991]) typically uses a single camera to obtain two-components of fluid velocity on a planar surface, with low to moderate temporal resolution. Stereoscopic

methods such as those in Arroyo and Greated (1991) and reviewed by Prasad (2000) use two cameras to obtain three-components of fluid velocity on a single planar surface. A generalized distortion compensation procedure employing calibration images is often used to map the image planes of the two cameras to the object plane in stereoscopic PIV (Soloff et al. 1997). This procedure allows for the recombination of two individual two-dimensional displacement fields (one from each camera) into a single three-dimensional displacement field. A variant of standard stereoscopic PIV called dual-plane stereoscopic PIV is described by Kähler and Kompenhans (2000). In the dual-plane configuration, stereoscopic PIV fields are recorded, instantaneously, on two parallel planes that are offset in the out-of-plane direction. Possession of velocity data on these two planes allows for the evaluation of derivatives in the out-of-plane direction.

Stereoscopic PIV (SPIV) requires a level of optical access that can be difficult to obtain in some experimental configurations. A hybrid method that uses PIV to obtain in-plane velocity components and Doppler global velocimetry (DGV) to obtain the out-of-plane velocity component has been described by both Wernet (2004) and Willert et al. (2006). While such a hybrid methodology may be different from stereoscopic PIV, the end result of three-dimensional velocity on a planar surface is similar.

A quasi-instantaneous volumetric method is obtained by using stereoscopic PIV with a laser sheet that is rapidly scanned in the out-of-plane direction, as applied to the case of a round turbulent jet by Hori and Sakakibara (2004). While the use of scanning does not strictly yield an instantaneous snapshot of the flow in the measurement volume, Hori and Sakakibara (2004) argued that since the scanning time was less than the Kolmogorov time scale, their method was adequate to resolve the smallest eddies in the flow. Another example of the use of a scanning stereoscopic PIV system was demonstrated by Burgmann et al. (2008). In their study, rather than mechanically scanning a single laser sheet with a mirror, ten independent laser heads, all pre-aligned at different out-of-plane locations, were fired in sequence. In this manner, a finite volume was rapidly illuminated and imaged.

One method capable of providing truly instantaneous volumetric data is holographic PIV (HPIV) (e.g. as used by Meng et al. 2004). HPIV illuminates a flow field seeded with particles, similar to standard PIV. An interference pattern is then recorded and interrogated to obtain three-dimensional displacements over a volume. Traditional HPIV uses photographic films as the recording medium. Given the time required to process films, the number of realizations that can be obtained is severely limited. Digital HPIV uses digital cameras as the recording medium.

However, the present inferior spatial resolution of a CCD array compared to photographic film limits the number of velocity vectors that can be obtained.

Other methods of obtaining instantaneous volumetric data include tomographic PIV (TomoPIV) (Elsinga et al. 2006; Schroder et al. 2008), defocusing digital PIV (DDPIV) (Willert and Gharib 1992; Pereira et al. 2000, 2006), and three-dimensional particle tracking velocimetry (3dPTV) (Maas et al. 1993; Virant and Dracos 1997; Pereira et al. 2006). TomoPIV uses diffuse laser light to illuminate seed particles over a volumetric region of interest. Scattered light from the seed particles is collected by an array (3–4) of cameras oriented at different angles. Three-dimensional particle distributions are reconstructed from the individual camera images and the distributions from the two camera exposures are cross-correlated to obtain the three-dimensional particle displacement field. DDPIV recovers depth information through the use of off-axis apertures. Finally, 3dPTV is similar to TomoPIV, but uses lower seeding densities, allowing individual particles to be tracked during the time interval between successive camera images.

The present paper describes volumetric three-component velocimetry (V3V) measurements of the flow in a cylindrical tank stirred by a Rushton turbine. The applied velocimetry method is based upon DDPIV and 3dPTV concepts. One aspect of its novelty is that it allows for higher seeding densities (and generates more velocity vectors) than previous 3dPTV studies. The Rushton turbine flow was chosen for two primary reasons. First, flows in stirred tanks are important to a wide range of engineering disciplines. Second, the flow is complex and highly three-dimensional, making it a suitable 'test case' for the volumetric measurements.

1.2 Rushton turbine flows: identification and characterization of tip vortices

Rushton turbines have been widely studied and used since the 1950s. They are high-shear devices that commonly find application to fluid dispersion and mixing processes. The literature on their power-consumption and flow-field characteristics is quite extensive and only the most relevant studies are discussed here. The flow field in a tank stirred by a Rushton turbine is characterized by a strong radial jet which sets up large ring vortices, one in each half (in the vertical sense) of the tank. In the absence of baffles, a strong circumferential flow will be established. Additionally, as discussed extensively in the literature beginning with the studies in the mid-1970s by van't Riet's group (1973, 1975, 1976), each blade produces a pair of counter-rotating tip vortices that promote mixing on a much smaller scale than the ring vortices.

The identification and characterization of the tip vortices is one specific aspect of Rushton turbine flows that is of particular interest in the present study. Various groups have constructed tip vortex trajectories for Reynolds numbers (*Re*) from 5,000 to 56,000 based on their velocity data (van't Riet and Smith 1975; Stoots and Calabrese 1995; Yianneskis et al. 1987; Lee and Yianneskis 1998; Derksen et al. 1999; Escudié et al. 2004). In the last decade, the use of extensive laser doppler anemometer (LDA) measurements (Bouremel et al. 2009b), individual planes of two-dimensional PIV data (Bouremel et al. 2009a), or multiple planes of two-dimensional PIV data (Escudié et al. 2004; Escudié and Liné 2007) in Rushton turbine flows has enabled some studies of tip vortex identification and characterization based on: (1) circumferential vorticity; (2) Jeong and Hussain's (1995) method of identifying pressure minima; and (3) the magnitudes of the principal components of the strain rate tensor, S_{11}^*, S_{22}^*, and S_{33}^*.

As introduced in Jeong and Hussain (1995) and reviewed in Escudié et al. (2004) with application to a Rushton turbine flow, the sign of the second eigenvalue of $\mathbf{S}^2 + \mathbf{\Omega}^2$ can be used to identify regions of pressure minima corresponding to vortex cores where $\mathbf{S}$ represents the (symmetric) deformation rate tensor and $\mathbf{\Omega}$ represents the (anti-symmetric) rotation rate tensor. More recently, the vorticity and strain dynamics of the tip vortices have been quantified using the magnitudes of the principal components of the strain rate tensor, S_{11}^*, S_{22}^*, and S_{33}^* as these components are measures of stretching and compression (Bouremel et al. 2009a, b).

The data acquired in the present Rushton turbine flow study represent the first set of three-dimensional data acquired with a volumetric measurement technique, and furthermore *the first set of volumetric data at multiple Re*, that can be used to compare the above methods plus the 'swirling strength' method (Zhou et al. 1999) applied to tip vortex characterization.

1.3 Previous PIV measurements in Rushton turbine flows

As far as previous use of PIV to study the flow around a Rushton turbine, a number of research groups have conducted two-dimensional PIV and three-dimensional in a plane (SPIV) measurements with varying research objectives (Sharp and Adrian 2001; Hill et al. 2000; Ranade et al. 2001; Escudié et al. 2004; Yoon et al. 2005; Ducci and Yianneskis 2007a, b). These previous studies, while limited to measurements in a plane, nevertheless provide a useful comparison with the current results.

As an example, one two-dimensional PIV experiment focused on the velocities and turbulence characteristics very near to the impeller, and used highly-resolved data to obtain estimates of dissipation rates (Sharp and Adrian 2001). These highly-resolved phase-locked data in the radial-azimuthal plane provided insight into the dynamics of the tip vortices (location, strength, etc.) as well as highly resolved maps of the mean and turbulent flow fields. Sharp and Adrian's (2001) data were acquired in a mixing tank with inner diameter, *D*, roughly 1/3 the inner diameter of the present tank, and with an experimental *Re* of approximately 4,000 as compared to 15,000–137,000 in the present experiments. Assuming some isotropy, these highly-resolved data formed the basis of dissipation maps in the near-blade region, and essentially represent two-dimensional slices from the type of three-dimensional data acquired presently (albeit with a smaller field-of-view and with a higher spatial resolution than these three-dimensional volumetric data).

An example of stereoscopic PIV measurements in the near-field of the impeller can be found in Hill et al. (2000). These stereoscopic data were interpolated onto a curved surface (the angular-axial plane) spanning two adjacent blade tips, providing a clearer picture of the three-dimensional structure of the tip vortices. Hill et al.'s (2000) work was extended by Yoon et al. (2005) in an effort to understand the scaling of the flow between differently sized tanks.

Clearly, the method used should reflect the research objective; the present PIV data provide a relatively global view of the tip vortex structure but are not highly-resolved enough to enable estimates of velocity gradients required for the calculation of dissipation. To effectively capture dissipation, PIV measurements should have a spatial resolution (and average over a window the size of) at most three times the Kolmogorov scale (Saarenrinne and Piirto 2000). In the present experiments, the spatial resolution ranges from approximately 10 to 50 times the Kolmogorov scale (for lowest to highest *Re* respectively) and any attempt to calculate dissipation would very severely underestimate the quantity. The tradeoff is that the present method has the ability to capture the full three-dimensional structure of not just the tip vortex pair from the closest blade, but also that of the preceding blade and even two blades prior for the highest *Re*.

Similarly, Yianneskis et al.'s (1987) use of photographic flow visualization and laser Doppler anemometry methods with the aim of quantifying the larger-scale circulations or so-called ring vortices in the tank is another example in which the measurement methods were tailored to the aim. Extensive 2-D PIV measurements in a series of orthogonal planes have also been used to characterize the tip vortices (Escudié et al. 2004), but the procedure was laborious and data limited to one *Re*. Again, while conventional PIV and stereoscopic PIV or other fluid mechanical diagnostic techniques can be tailored to allow for acquisition of

specific types of data, if a more global view of a highly three-dimensional flow is desired, volumetric three-dimensional velocimetry offers a useful alternative.

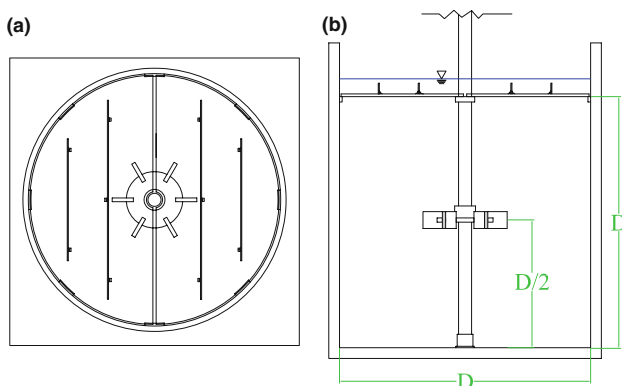## 2 Experimental methods and procedure

2.1 Tank and turbine geometry

The present experiments were conducted in an unbaffled cylindrical mixing tank (Fig. 1) with an inner diameter (D) of 44.3 cm. The tank was filled with water to a depth equal to D and a lid was used to prevent free surface displacement (Froude number effects) and to help ensure vertical symmetry in the mixing tank. The cylindrical tank was then placed in a square glass tank of larger dimension and the space between the two tanks was filled with water. This was done to greatly reduce refraction from the outer curved surface of the cylindrical tank.

Mixing in the tank was provided by the rotation of a six-blade Rushton turbine, located at the vertical midpoint of the tank. The turbine followed the traditional specification of having a diameter (blade tip to blade tip; D_T) equal to $D/3$. In a slight variation from the usual configuration, the impeller shaft passed through the impeller disk and extended to the bottom of the tank, where it was supported by a bearing. This was done in an effort to minimize lateral oscillations of the shaft at high rotational rates and ensure vertical symmetry. The impeller was controlled by a mixer (Lightnin, Inc., L5U10F) and was painted a flat black in order to reduce reflections of laser light.

In the present experiments, data were obtained at impeller rotational speeds of 42, 295, and 379 rpm. For impeller flows, the Re is generally defined as

$$Re = \frac{ND_T^2}{v} \tag{1}$$

where N is the rotational rate in revolutions per second and v is the fluid's kinematic viscosity. Therefore, the present data sets correspond to Re values of approximately 15,000, 107,000, and 137,000.

2.2 Data acquisition

The flow field was illuminated from the side with a dual-head Nd:Yag laser emitting light with a wavelength of 532 nm, a pulse width of 12 ns, and energy of 120 mJ pulse^{-1}. The two beams were combined to travel on co-linear paths. A light cone was generated with two −25 mm cylindrical lenses that were mounted so that their axes of transmission were 90° to each other. These cylindrical lenses spread the beam in the horizontal and vertical directions to illuminate a measurement volume approximately 120 mm height by 120 mm width by 100 mm depth. Beam blocks were placed at the edge of the rectangular water tank in order to clip the laser cone to illuminate only the volume depth being measured and reduce background noise. The flow was seeded with Optimage polycrystalline particles (mean particle diameter $\overline{d_p} = 100\,\mu m$), with specific gravity approximately equal to one.

The V3V camera probe (TSI, Inc.), shown in Fig. 2, consists of three apertures, each containing 4 million pixels
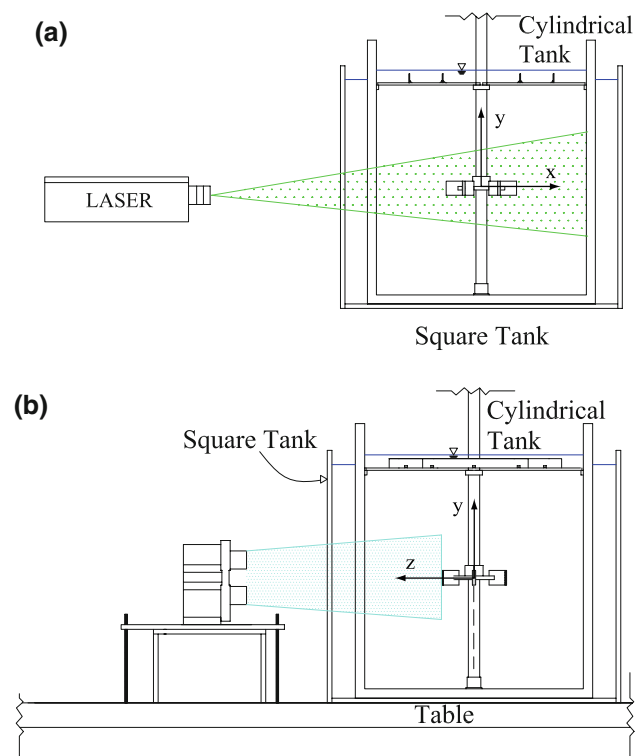

Fig. 2 a Front elevation view (as seen by camera) and **b** side elevation view of experimental tank, showing location of laser, camera, turbine, and illuminated region

Fig. 1 a Plan and **b** elevation views of the experimental tank

(2,048 × 2,048). The images are 12 bits, with a pixel size of 7.4 μm. Fifty mm camera lenses were used with a fixed aperture of f16. The V3V camera frames and laser pulses were triggered by a TSI 610035 synchronizer with 1 ns resolution. The pulses from each laser were timed to straddle neighboring camera frames in order to produce images suitable for 3D particle tracking. The time between frame-straddled laser pulses (Δt) was 1,500, 250, and 200 μs, for the speeds of 42, 295, and 379 rpm, respectively. The synchronizer was externally triggered by a shaft encoding trigger mounted on the shaft of the turbine axis. This allowed velocity captures to be taken consistently at the same phase in the shaft cycle. The images were streamed to a HYPER2 HyperStreaming computer, and subsequently analyzed.

2.3 Data processing

The 3D particle tracking algorithm consists of a relaxation method based upon the work of Ohmi and Li (2000) and improved upon by Pereira et al. (2006). It is done in three primary steps. The first is determining the 2D particle locations in each image, then determining the 3D particle locations in space, then tracking the particles in the volume.

For each capture, the 2D particles in the six separate images were identified with a global threshold of 100 out of 4,096 grayscales and a radius of between 2 and 4 pixels. Particles not falling within this criteria were eliminated. A Gaussian intensity peak was fitted to each particle, and 3D particle identification was performed, where particle locations from each of the three image locations were compared against the calibration and combined to find the 3D particle location, or triplet. The centroids of the 2D particle locations were forced to match the calibration to within a tolerance of 0.5 pixels. Figure 3 shows a schematic
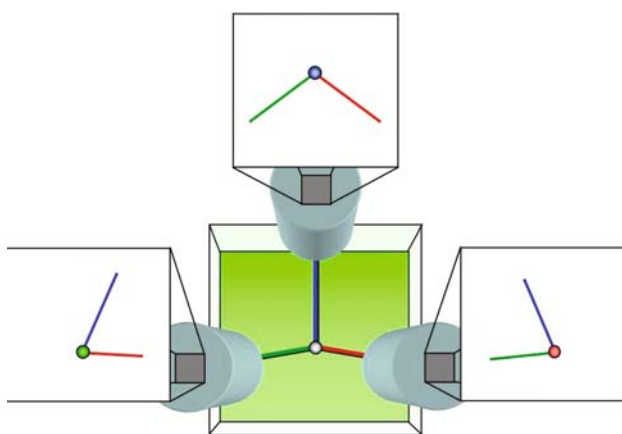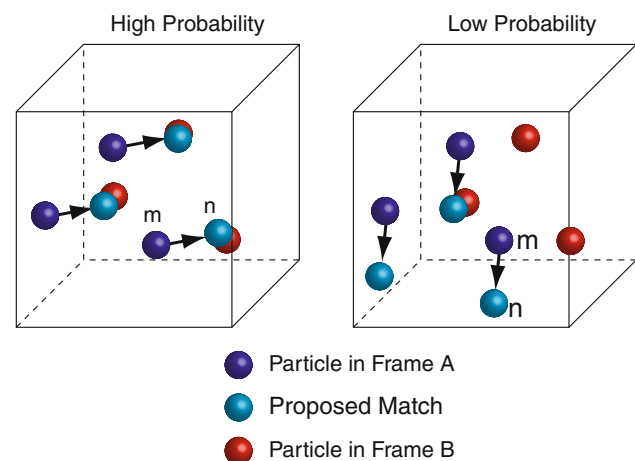
representation of the triplet matching, in which a particle in one of the images defines a ray in the other two images, along which the search is done. When suitable matches are found in all three images to within the tolerance, a triplet is achieved. After the particle clouds are achieved for both times t and $t + \Delta t$, a relaxation method of particle tracking was performed. The technique is described well by Pereira et al. (2006), in which particles are divided into clusters; clusters in the second frame are larger than those in the first frame. Each particle match is assigned a probability based on the assumption that neighboring particles move similarly. The probabilities are iteratively recomputed for all particles in the cluster until they converge. Figure 4 shows a schematic representation of the particle tracking step.

After the 3D particle tracking step, the vectors lie on a randomly spaced grid, according to particle locations. In order to compute quantities such as vorticity, it is useful to have vectors on a rectangular grid. This was done through regular Gaussian-weighted interpolation. For the experiments carried out here, the average number of 2D particles identified per image was approximately 60,000 which resulted in approximately 30,000 valid 3D particles. Of these particles, the average number of independent particle-tracked vectors was approximately 15,000. These randomly spaced vectors were interpolated onto a rectangular grid with 4 mm vector spacing which resulted in an average of approximately 23,000 vectors per field. For each Re, 250 phase-locked realizations were obtained, and the velocity fields were ensemble-averaged to yield mean and turbulent flow fields.

The data were post-processed in the Cartesian coordinate system to yield quantities such as vorticity and turbulent kinetic energy. Vorticity was decomposed into its radial-circumferential-axial components, as these provide a more insightful perspective, but the components remain

Fig. 3 Schematic of V3V aperture arrangement and the 2d representations of a single particle and the optical rays from all three cameras

Fig. 4 Illustration of potential (high probability and low probability) particle matches between successive camera frames

plotted on a rectangular Cartesian grid in Figs. 5, 6, and 7. This volume of data is 'sliced' at six phase angles defined in terms of the number of degrees past blade passage ($\theta = 0°$–$50°$) to enable more detailed analysis of the flow.

The uncertainty in velocity relates primarily to the accuracy with which the 3D particle locations are determined and is discussed at length by Pereira et al. (2006). For the current set of experiments, the velocity uncertainty for the instantaneous vector fields was 2% in x and y, and 8% in z. Outlier detection was performed on the randomly-spaced velocity fields through a global velocity filter and a local normalized median filter. Each velocity field consisted of 98% or higher valid vectors.

3 Experimental results and discussion

## 3.1 Mean vorticity, mean velocity, and turbulent kinetic energy in the volume

Figure 5 gives results for the mean, non-dimensionalized, angular vorticity, ω_θ^*, for the 295 rpm case ($Re \sim 107,000$), calculated using a simple central difference method. Note that the impeller diameter and the blade tip speed have been used as characteristic length and velocity scales in normalizing these and all subsequent results. An asterisk

symbol is used to denote scaled variables. Next, note that the impeller is displayed in order to help establish the relative position of the volumetric data region. The origin of the coordinate system is at $(x^*, y^*, z^*) = (0, 0, 0)$ or $(r^*, \theta, y^*) = (0, 0, 0)$. The heavy gray line indicates the axis of the impeller shaft and the angular velocity vector of the impeller is aligned with the negative y axis. In Figs. 5, 6, and 7 as drawn, the turbine is rotating in the clockwise direction. Isosurfaces of angular vorticity are shown, clearly revealing the structure of the counter-rotating tip vortices. Two pairs of tip vortices are present, as shed from adjacent impeller blades. Vertical slices of angular vorticity are also included, showing the rapid radial decay of the fluid vorticity.

Similar perspective views of the mean velocity field are given in Fig. 6, also for $Re \sim 107,000$. The vorticity isosurfaces from Fig. 5 are retained and one new isosurface of normalized fluid speed is presented. From this latter surface, the Gaussian profile of the radial jet becomes quite evident. Velocity vectors are also shown and indicate the strong circumferential flow established in the non-baffled experimental tank. Note that only every third vector in each of the three Cartesian directions is shown for the sake of visual clarity.

Figure 7 presents results for the turbulent kinetic energy, tke*, defined as

Fig. 5 Isosurfaces and vertical slices of mean, normalized angular vorticity (ω_θ^*) for the 295 rpm case ($Re \sim 107,000$)
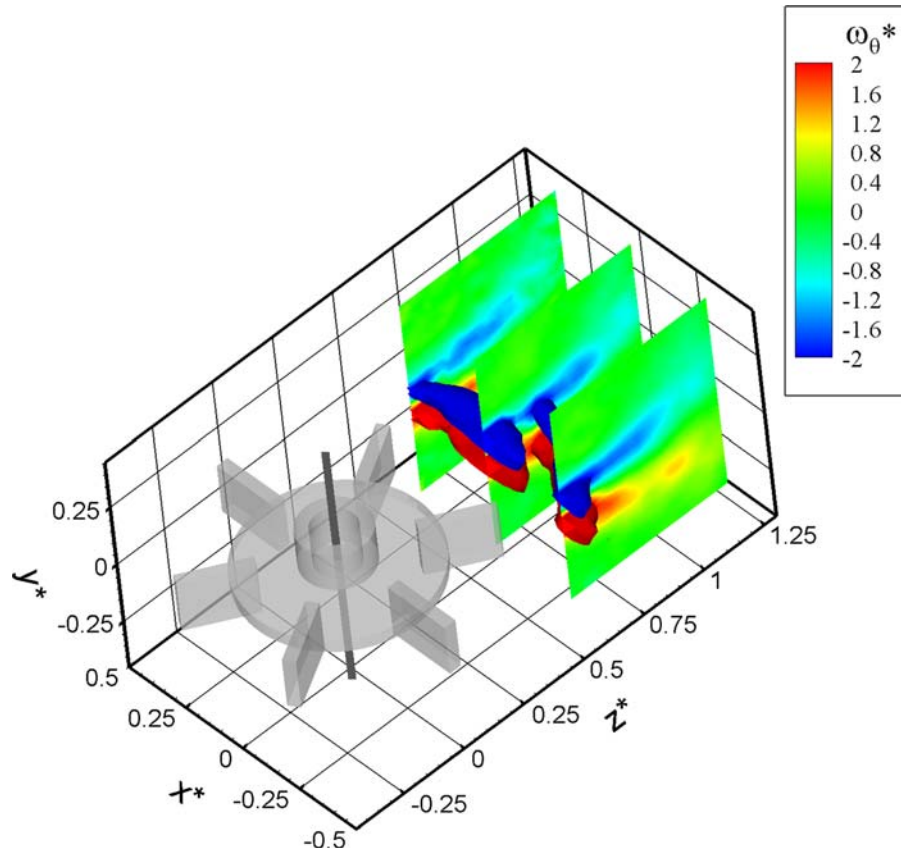
Fig. 6 Isosurface of mean, normalized fluid speed for the 295 rpm case ($Re \sim 107{,}000$). The isosurfaces of mean vorticity are also shown to indicate the locations of the tip vortices, and vectors of the mean velocity field displayed to show three-dimensional nature of measurements
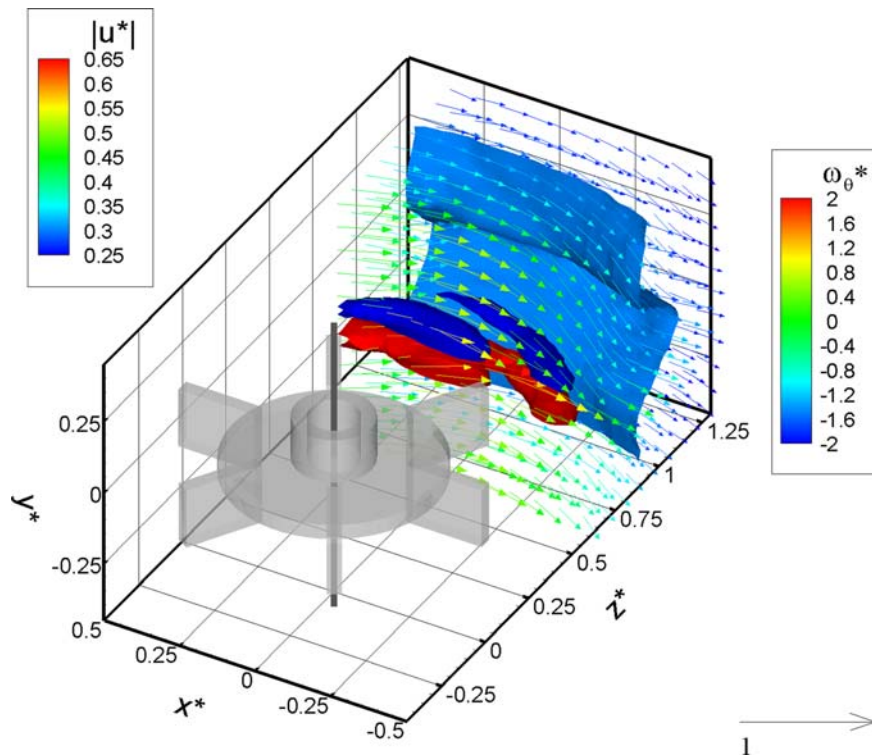

$$\text{tke}^* = \frac{1}{2}\left(\langle u'u'\rangle^* + \langle v'v'\rangle^* + \langle w'w'\rangle^*\right) \qquad (2)$$

where u', v' and w' represent the fluctuations from the phase-locked mean field.

As with the mean flow data, flow variables have been non-dimensionalized by using the impeller diameter and the blade tip velocity as characteristic length and velocity scales. Select slices through the data volume and

Fig. 7 Computed normalized turbulent kinetic energy for 295 rpm experiment ($Re \sim 107{,}000$). Isosurfaces of tke* are shown along with tke* at three vertical slices and one horizontal slice
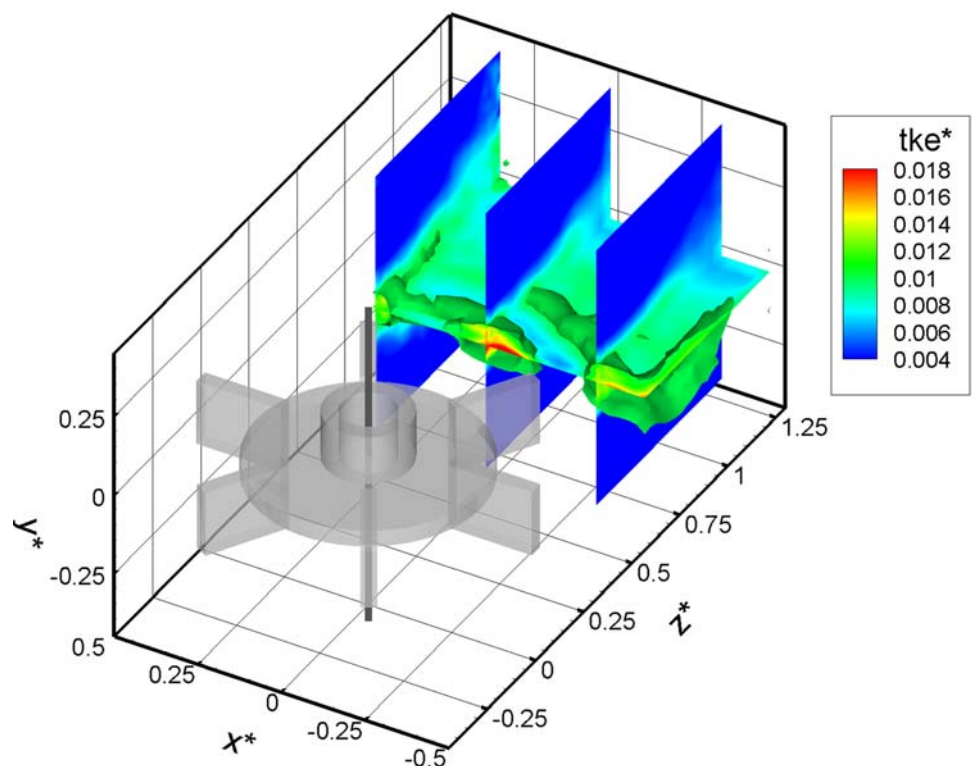
isosurfaces have been used to bring out the key characteristics of the distributions. For the turbulent kinetic energy, values outside of the radial jet are extremely small and the peak values are found on the vertical center-plane, not in the tip vortex cores. In fact, each tip vortex pair merges into a single concentrated region of high turbulent kinetic energy. While straight ensemble-averaging was used to calculate the fluctuating velocities in the three-dimensional volume, the mean field is essentially phase-locked since each realization of three-dimensional data was taken at the same blade position. The radial location of approximately $r^* = \sqrt{x^{*2} + z^{*2}} = r/D_T \sim 0.6$ for peak turbulent kinetic energy compares well with previously published angle-resolved turbulent kinetic energy results such as those in Lee and Yianneskis (1998).

3.2 Tip vortex identification

After the data are interpolated onto a regular grid in the volumetric data acquisition region, 'slices' can be taken at horizontal, vertical, or constant-θ planes. For much of the quantitative analysis of tip vortex structure and trajectory, it is useful to have data at a series of constant-θ planes at 10° increments. A top view of the measurement volume and the slices is shown in Fig. 8. For the 0° and 50° slices, there are fewer datapoints in each plane, given the rectangular geometry of the measurement volume.

To investigate the tip vortex location and structure on each of these planes, it is helpful to calculate both a non-dimensionalized circumferential vorticity, ω_θ^*, and to
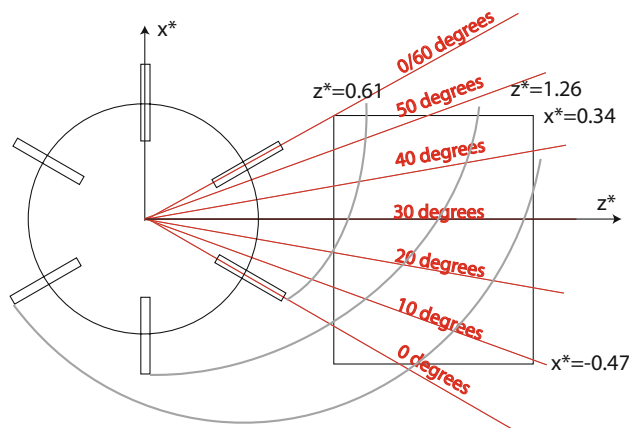
Fig. 8 Schematic of measurement volume and constant-θ planes used for extraction of 'slice' data. Note that the 'degrees past blade passage' shown is the degrees past passage of the most recently-passed blade. Thus, the 0° past blade passage also corresponds to 60° past passage of the blade two prior, and 120° past passage of the blade three prior. Approximate vortex trajectories are sketched in to orient the reader. Note that only for the highest Re can an isosurface of the tip vortex three blades prior be readily visualized in the measurement volume

consider identifying the tip vortex either by arbitrarily setting a threshold for the magnitude of the non-dimensional angular vorticity, ω_θ^*, by using the 'λ_2' definition of a vortex structure attributed to Jeong and Hussain (1995), or by using a swirl strength criterion as described in Zhou et al. (1999). For the method proposed by Jeong and Hussain (1995), the pressure is related to the deformation rate tensor, S_{ij}, and the rotation rate tensor, Ω_{ij} by

$$\Omega_{ik}\Omega_{kj} + S_{ik}S_{kj} = -\frac{1}{\rho}p_{,ij} \qquad (3)$$

where

$$S_{ij} = \frac{1}{2}\left(\frac{\partial u_i}{\partial x_j} + \frac{\partial u_j}{\partial x_i}\right) \qquad (4)$$

and

$$\Omega_{ij} = \frac{1}{2}\left(\frac{\partial u_i}{\partial x_j} - \frac{\partial u_j}{\partial x_i}\right) \qquad (5)$$

where u_i represents velocity, x_i represents position, p represents pressure, and ρ represents density. If the eigenvalues of the tensor $\mathbf{S^2} + \mathbf{\Omega^2}$ are ordered by $\lambda_1 \geq \lambda_2 \geq \lambda_3$, then presupposing that the existence of a vortex region can be delineated based on the existence of a local pressure minimum, it follows that a vortex core is associated with $\lambda_2 < 0$ (Jeong and Hussain 1995). The full three-dimensional velocity gradient tensor is used in the first calculation of λ_2. (The use of two-dimensional and three-dimensional velocity data for vortex identification methods is addressed later).

The swirl strength criterion as introduced by Zhou et al. (1999) recognizes that the velocity gradient tensor can be decomposed in terms of its eigenvalues and eigenvectors. Representing the velocity gradient tensor as $\mathbf{D}$, it follows that

$$\mathbf{D} \equiv [d_{ij}] = [\mathbf{v_r}\mathbf{v_{cr}}\mathbf{v_{ci}}]\begin{bmatrix} \lambda_r & & \\ & \lambda_{cr} & \lambda_{ci} \\ & -\lambda_{ci} & \lambda_{cr} \end{bmatrix}[\mathbf{v_r}\mathbf{v_{cr}}\mathbf{v_{ci}}]^{-1} \qquad (6)$$

where the real eigenvalue and eigenvector are represented by λ_r and $\mathbf{v_r}$ respectively, and the complex eigenvalues and corresponding eigenvectors are represented by $\lambda_{cr} \pm i\lambda_{ci}$ and $\mathbf{v_{cr}} \pm i\mathbf{v_{ci}}$. Given the above decomposition, Zhou et al. (1999) deduced that, along the $\mathbf{v_r}$ axis, the flow is stretched or compressed but in the $\mathbf{v_{cr}} - \mathbf{v_{ci}}$ plane, the flow is swirling. Furthermore, λ_{ci} is deemed a measure of the local swirling strength and thus its magnitude (or the magnitude of its square) can be used to locally identify vortices.

In order to compare the above-described methods of tip vortex identification, the non-dimensionalized circumferential vorticity (ω_θ^*), the value of the second eigenvalue of the $\mathbf{S^2} + \mathbf{\Omega^2}$ tensor (λ_2) and the value of the complex eigenvalue of $\mathbf{D}$ (λ_{ci}) are calculated from the

Fig. 9 Isosurfaces of **a** $\omega_\theta^* = 2, -2$, **b** $\lambda_2 = -0.15$, and **c** $\lambda_{ci}^2 = 0.56$ showing comparison of methods used to identify tip vortices in flow with $Re \sim 15,000$
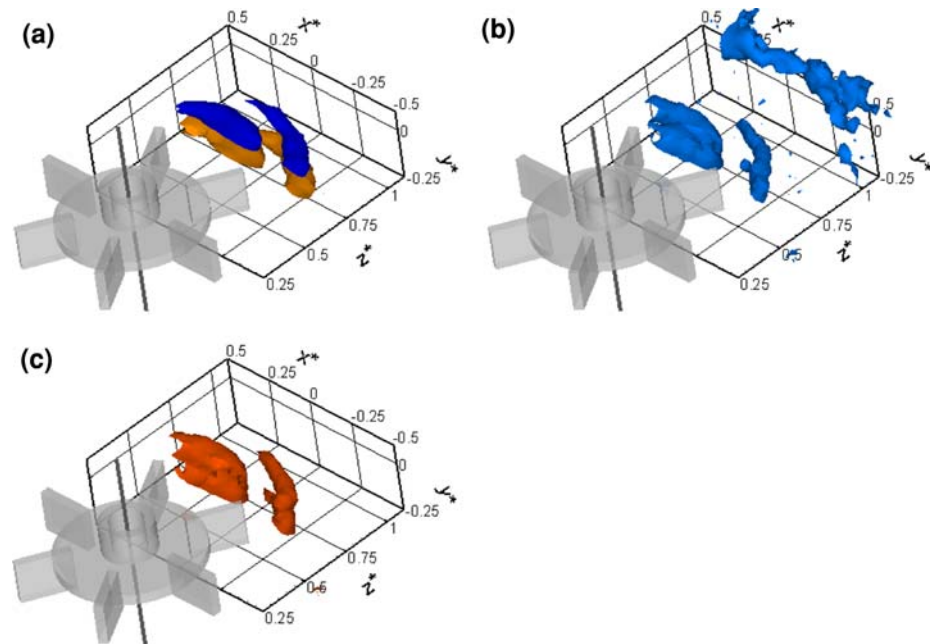

three-dimensional velocity data for the lowest Re case ($Re \sim 15,000$). Isosurfaces of values of $\omega_\theta^* = 2$ and $\omega_\theta^* = -2$ are shown in Fig. 9a, an isosurface of $\lambda_2 = -0.15$ is shown in Fig. 9b, and an isosurface of $\lambda_{ci}^2 = 0.56$ is shown in Fig. 9c. The values of each of these measures are somewhat arbitrary and selected to enable this particular comparison. Each measure serves to identify both top and bottom vortices shed off of the just-passed blade and the blade prior, where the blade prior is nearly aligned with $z^* = 0.25$ in the displayed view. The diameter of the identified tip vortex core varies slightly from (a–c), however, the diameter of the isosurface defining the core depends on the numerical (and often somewhat arbitrary) value of the isosurface level.

The primary intent of Fig. 9 is to show the structural similarities of tip vortices identified using three different methods. A secondary intent is to demonstrate that even using the arbitrary value of $\lambda_2 = -0.15$ (more restrictive than $\lambda_2 < 0$ which is strictly speaking the measure defined by Jeong and Hussain (1995)'s pressure minimum criterion), isosurfaces also appear towards the outer edge of the measurement volume. It is possible that the isosurfaces in these outer regions represent residual vorticity in the tank well outside of the tip vortices, but the unstructured nature suggests either measurement noise leading to noise in the calculation of λ_2 or that λ_2 is not the best method of tip vortex identification in the present flow. Interestingly, these additional isosurfaces in the outer region of the measurement volume are not present when isosurfaces of λ_{ci}^2 are drawn.

Additional visual comparisons of the vortex identification methods are shown in Figs. 10 and 11, again for

$Re \sim 15,000$. Figure 10 shows a two-dimensional slice of data at $\theta = 20°$ past blade passage. Here the coloring represents ω_θ^*, the black contour lines show levels of $\lambda_2 = 0$ and -0.15, and white contour lines show $\lambda_{ci}^2 = 0.28$, 0.56, and 0.84 corresponding to 1.4, 2.8, and 4.2% of the maximum value of λ_{ci}^2 (as in Zhou et al. (1999)). As expected, the physical extent of the tip vortex 'core' depends on the level selected for each of these
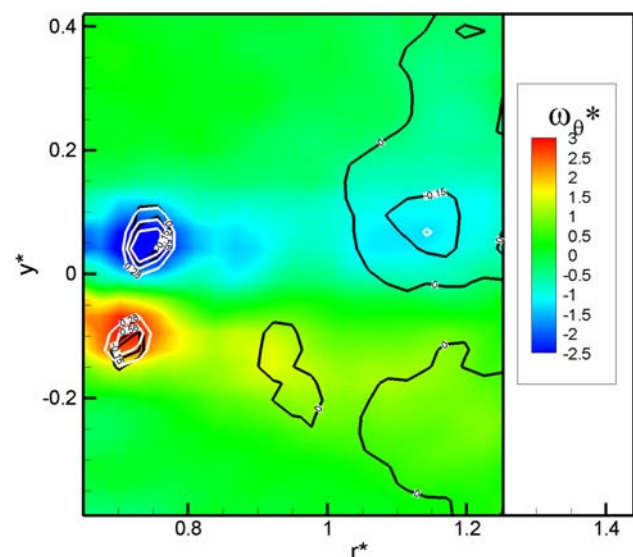
Fig. 10 Comparison of mean, normalized angular vorticity and contour levels for $Re \sim 15,000$ case. Black contour levels are drawn at $\lambda_2 = 0$ and -0.15 and white contour levels are drawn at $\lambda_{ci}^2 = 0.28$ 0.56, and 0.84 corresponding to 1.4, 2.8 and 4.2% of maximum value of λ_{ci}^2

measures, but the center of the region identified as a tip vortex core remains relatively consistent within and between each measure. The most notable difference between the measures is that $\lambda_2 = 0$ or -0.15 is less able to differentiate the tip vortex from either noise or residual vorticity towards the outside of the measurement volume.

Similar contours of non-dimensionalized angular vorticity, cutoff for $\lambda_2 = 0$, and cutoff for $\lambda_{ci}^2 = 0.56$ calculated using the three-dimensional velocity data in the 42 rpm case ($Re \sim 15,000$) for sequential planes past blade passage are shown in Fig. 11. Note that in frames (a–d) of Fig. 11, the primary vortex pair with radial position around $r^* \sim 0.7$–0.8 is actually the one shed off the previous blade, i.e. this counter-rotating pair of vortices is (a) 60°, (b) 70°, (c) 80°, and (d) 90° past blade passage. It is seen in Fig. 11 that for the counter-rotating vortices at 60–80° past blade passage (frames (a–c)), the λ_2 and λ_{ci}^2 methods of vortex identification roughly track what appear to be the vortex cores. In frame (d), this same pair is now 90° behind its source blade, and the pair off the more-recently-passed blade is just beginning to appear in the left-hand-side of the frame. (The pair shed off the most-recently-passed blade has a radial position, $r^* < 0.68$, the inner limit of the measurement volume in frames (a–c)). In frames (e) and (f), the pair at 100° and 110° past its source blade no longer retains enough vortical strength to be identified using a λ_2 or λ_{ci}^2 criterion. In frames (b–f), there are some additional regions at $r^* > 1$ that are identified as 'vortex-containing' using the λ_2 cutoff as in Fig. 10. A reasonable cutoff for delineation of the magnitude of the non-dimensionalized vorticity in the tip vortex is approximately 2.5–3. This is in of the same order of magnitude as the cut-off of approximately 4.3 used by Schäfer et al. (2000) but one order of magnitude smaller than the cutoff of approximately 12–19 used by Escudié et al. (2004). As pointed out by Escudié et al. (2004), the arbitrary cutoff can vary depending upon slice position, and it is relatively easy to under or overestimate the region of the vortex, thus many groups prefer the 'λ_2' or 'swirl strength' (λ_{ci}^2) method, but these methods do require substantially more velocity data.

According to the calculations shown in Figs. 9, 10, and 11, swirl strength is a better method of delineating tip vortices in a Rushton turbine flow. and is thus relied upon to identify the center of the tip vortices for the trajectory analyses. In all cases, the center of the vortex identified by λ_{ci}^2 was compared visually to the center of the region of vorticity concentration, with less than a $\pm 2.5\%$ difference in physical location. Also, despite the extent of the tip vortex core depending upon the actual numerical value of the λ_{ci}^2 contour, the location of the *center* does not vary with level.
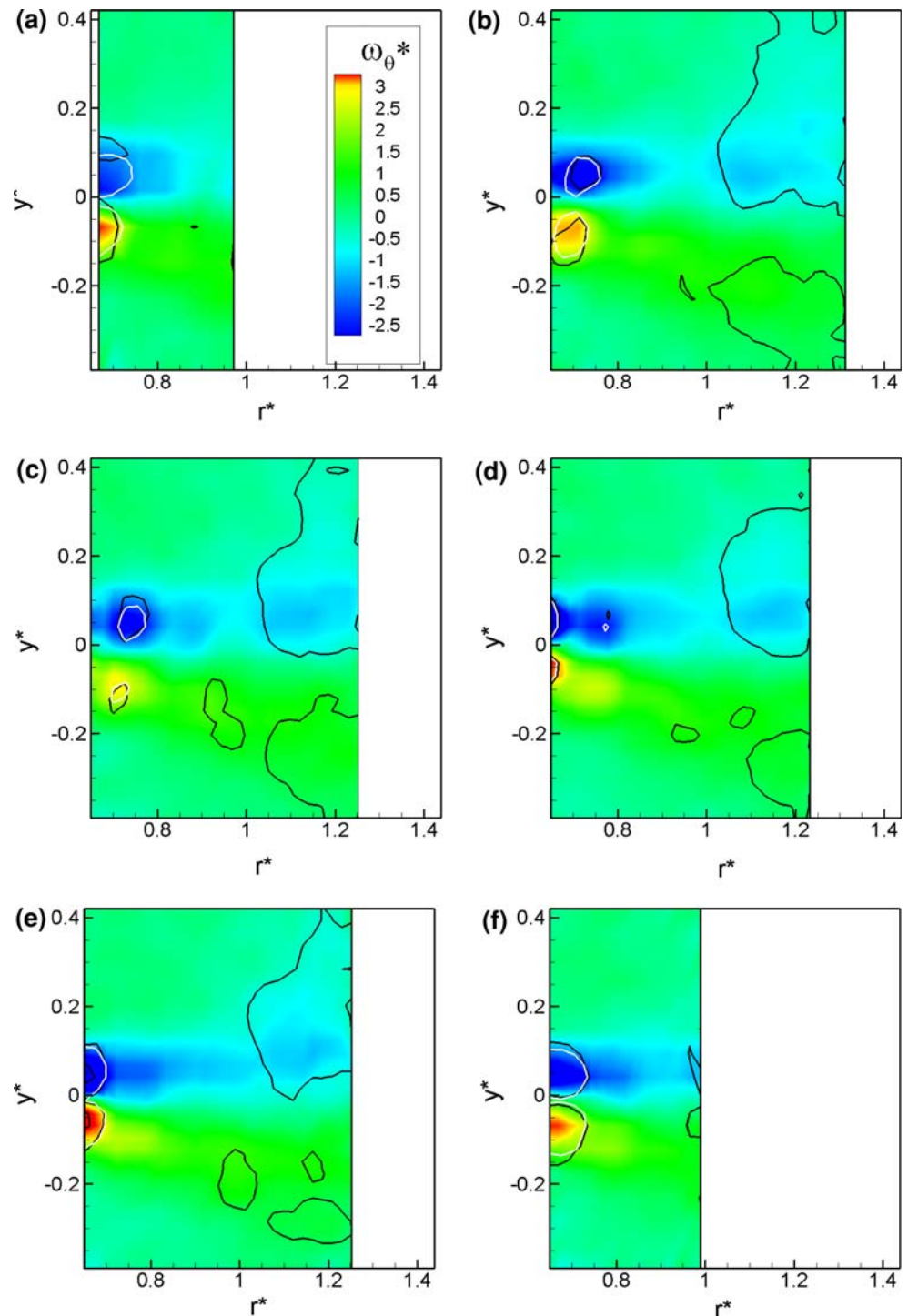
3.3 Use of two-dimensional versus three-dimensional data for tip vortex identification

In Escudié et al's (2004) study, two-dimensional PIV measurements were laboriously conducted in 19 planes in a Rushton turbine flow in order to obtain the out-of-plane velocity gradients required for computation of S_{ij} and Ω_{ij}. These 19 planes included one radial–axial (vertical, r–y) plane, nine vertical-tangential planes and nine horizontal planes. Each of the orthogonal planes intersects the primary radial–axial plane. The result was a grid of mean data spaced every 1.1 mm in the primary radial-axial plane, plus 9 lines in y (spaced every 5 mm), and 9 lines in r (spaced every 5 mm). Out-of-plane velocity gradients were calculated along these lines in y and r. With three-dimensional velocity gradient data at a limited but reasonable number of points, Escudié et al. (2004) proceeded to use the standard λ_2 method to identify the location of the tip vortices.

Since three-dimensional velocity data on a three-dimensional grid has, until recently, been relatively difficult and laborious to obtain, more recently a method for identifying vortices using the $\lambda_2 < 0$ criterion based only on two-dimensional planar velocity gradient data was introduced by Escudié and Liné (2007). Using a single plane of two-dimensional PIV velocity data, Escudié and Liné (2007) estimated an out-of-plane velocity gradient tensor component based on application of the continuity equation. Using their new method with just two-dimensional data in the vertical plane enabled tip vortex identification with very similar results when compared with tip vortex identification based on three-dimensional data (Escudié and Liné 2007). The two-dimensional procedure resulted in a slightly smaller region being identified as a vortex, but the difference between the two might be considered acceptable given the dramatic reduction in experimental and computational cost.

A similar comparison, following Escudié and Liné (2007), has been conducted with the present fully-three dimensional data and two-dimensional 'slices', with the calculation of both λ_2 and λ_{ci}^2. The comparison is shown in Fig. 12 for $Re \sim 15,000$ and for sequential planes past blade passage. In frames (a)–(d), the vortex pair is actually the one shed off the previous blade, i.e. this set of vortices is (a) 60°, (b) 70°, (c) 80°, and (d) 90° past blade passage. The pair shed off the most-recently-passed blade is not first detected in the measurement volume until frame (d) and is more visible at the inner edge of the measurement volume in frames (e) and (f). Interestingly, contrary to Escudié and Liné's (2007) conclusions, here there is a marked difference in the boundary where $\lambda_2 = 0$ even in frames (d–f) and for $r^* < 1$ where the strongest tip vortices are seen. However, identification of regions with high swirling

Fig. 11 Contours of mean, normalized angular vorticity in 42 RPM (*Re* ∼ 15,000). *Black* contour levels are drawn at $\lambda_2 = 0$ and *white* contour levels are drawn at $\lambda_{ci}^2 = 0.56$ (2.8% of maximum value of λ_{ci}^2) **a** 0°, **b** 10°, **c** 20°, **d** 30°, **e** 40°, **f** 50°


strength (λ_{ci}^2) is much more consistent regardless of the use of two- or three-dimensional data.

3.4 Principal strain rates as a measure of stretching or compression

Very recently, the calculation of principal strain rates in a region close to a Rushton turbine has been used to investigate deformation dynamics in the tip vortex region (Bouremel et al. 2009a, b). Essentially, the strain rate tensor, **S**, can be expressed in terms of its eigenvalues and eigenvectors, where each eigenvector and eigenvalue pair gives both a ω measure of stretching (positive) or compression (negative) and the direction along the three orthogonal principal axes. The principal strain rates are represented by S_{11}^*, S_{22}^*, and S_{33}^*.

Fig. 12 Contours showing cutoff of $\lambda_2 = 0$ computed using 3D velocity data (*black*), $\lambda_2 = 0$ computed using 2D velocity data (*grey*), $\lambda_{ci}^2 = 0.56$ where 0.56 represents 2.8% of maximum λ_{ci} computed using 3D velocity data (*red solid*), and $\lambda_{ci}^2 = 0.56$ computed using 2D velocity data (*red dotted*) in 42 RPM case ($Re \sim 15{,}000$) at sequential planes past blade passage: **a** 0°, **b** 10°, **c** 20°, **d** 30°, **e** 40°, **f** 50°
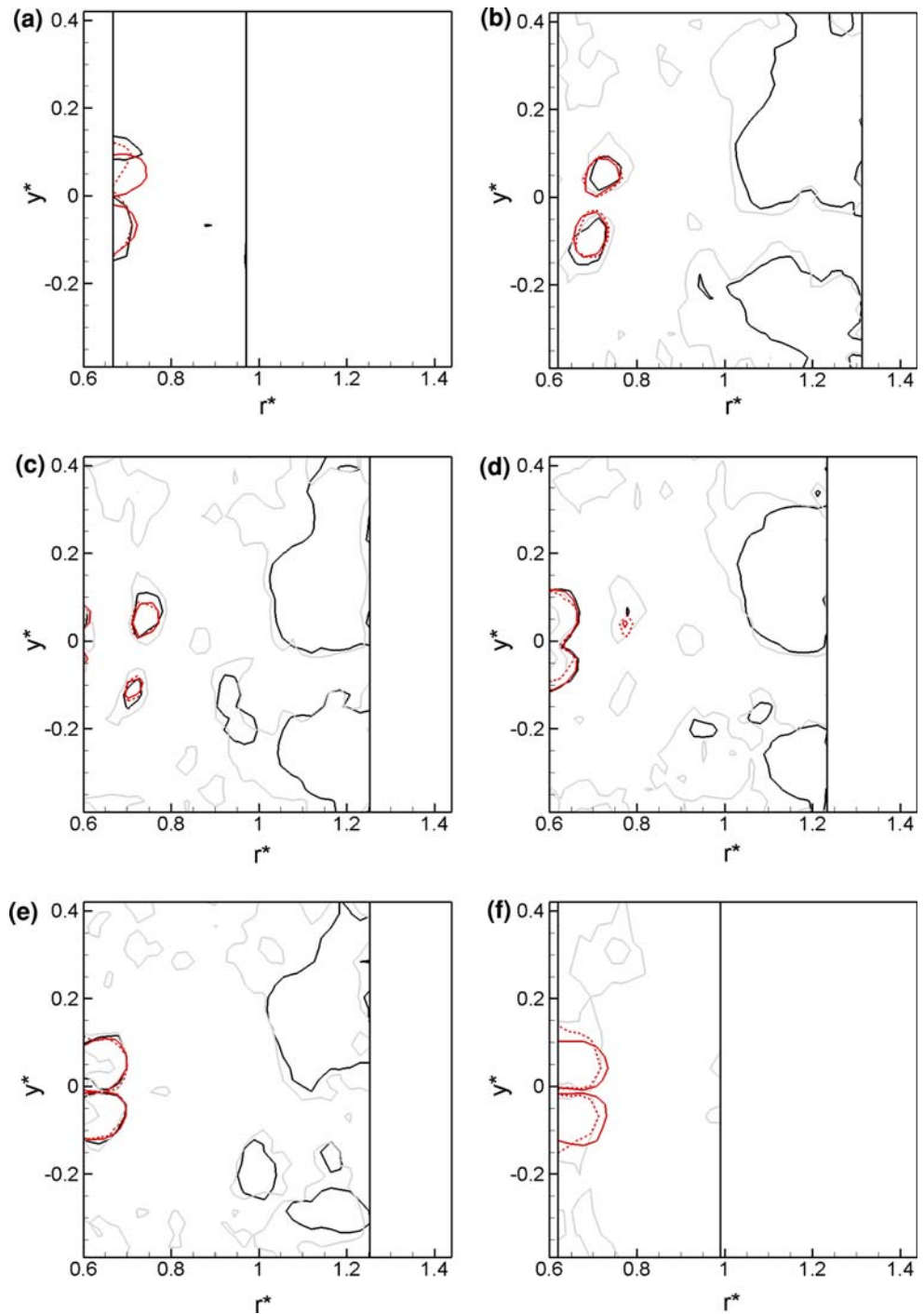

The first datasets used in a Rushton turbine tank for such calculations were obtained using LDA and were acquired at $Re \sim 2{,}780$. An extensive discussion of the results using three-dimensional LDA data appears in Bouremel et al. (2009b). These same principal strain rates are calculated using the present three-dimensional PIV data, and slices of the individual rates plus the triple product ($S_{11}^* \times S_{22}^* \times S_{33}^*$) are plotted in Fig. 13 for comparison with Figs. 9 and 10, Bouremel et al. (2009b).

Similar to Bouremel et al. (2009b), S_{11}^* is always negative representing compression, S_{33}^* is always positive representing stretching, and S_{22}^* is both positive and negative but is generally smaller or less dominant than the other two strain rates. At a vertical location of $y^* = 0.08$ (just above the middle of the vortex), the peak S_{11}^* occurs at the edge of the tip vortex structure. It is less clear but possible that the peak S_{33}^* occurs at the edge of the tip vortex structure as put forth by Bouremel et al. (2009b). The lack

Fig. 13 Slices of principal strain rates shown at $y^* = 0$ (*centerline*) and $y^* = 0.08$ for $Re \sim 15{,}000$. For reference, the top edge of the blade is at $y^* = 0.1$. **a** S_{11}^*, **b** S_{22}^*, **c** S_{33}^*, **d** $S_{11}^* \times S_{22}^* \times S_{33}^*$
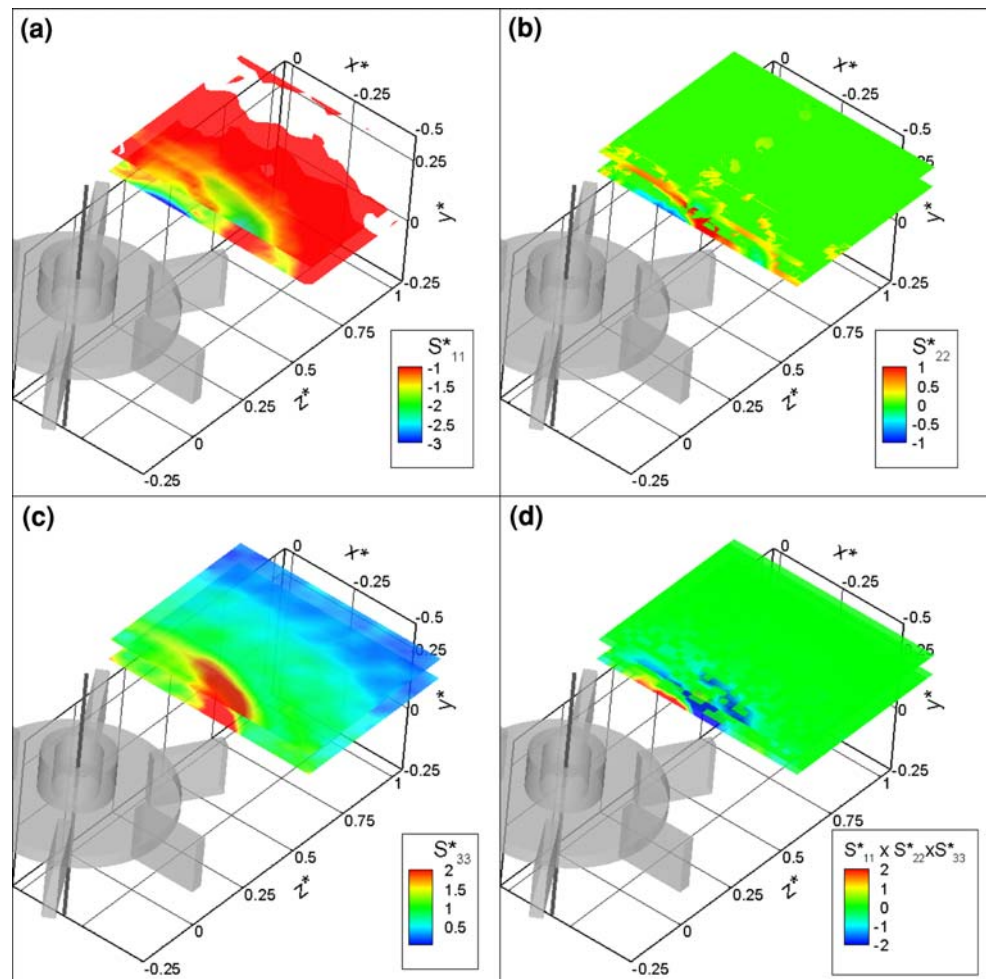
of clarity is primarily attributed to the fact that the present measurement volume sits considerably further out in the radial direction with a minimum $r^* > 0.6$ (outside of the edge of the blades) rather than the $r^* \sim 0.2$ (in between blades) achieved by Bouremel et al. (2009b) with their LDA measurements. The triple product (Fig. 13d) is strongest at the centerline.

While the calculation of principal strain rates can indeed be performed using the present three-dimensional data and the results appear reasonably consistent with the trends observed in Bouremel et al. (2009b), the location of the measurement volume further away from the blades (in r^*) means that the strain rates are less useful for actually identifying the tip vortices. A comprehensive analysis of the results and comparison remain outside the scope of the present paper.
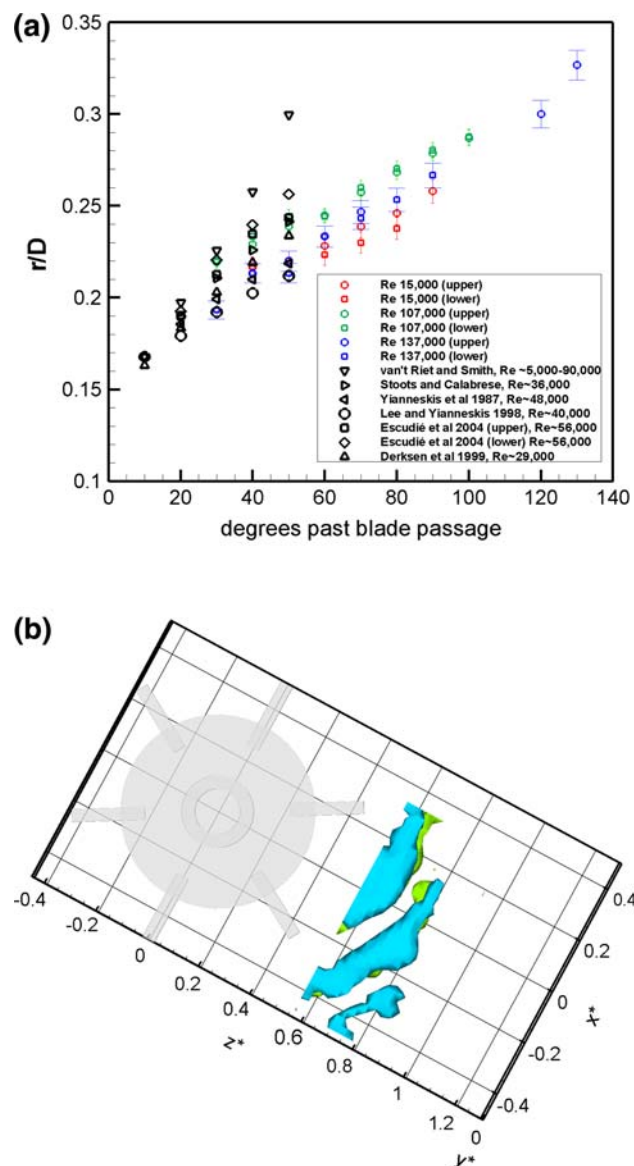
3.5 Trajectory and strength analysis

Having characterized the tip vortices for three Re as a function of position past blade passage, a comparison of tip vortex trajectories for these three Re to trajectories found in the literature is compiled in terms of r/D, where r is the radial position of the center of the vortex and D is the tank diameter measured versus degrees past blade passage (Fig. 14a). Both upper and lower vortex trajectories are shown where available. The position of the vortex centers was estimated as the middle of the region identified as a vortex by $\lambda_{ci}^2 = C$ where C is 0.14 or 0.56 (0.7 or 2.8% of its maximum within the field of view, based upon λ_{ci}^2 levels used to visualize vortices in Zhou et al. (1999)) and supported by the circumferential vorticity contours. Note that the 'center' of the vortex depends little on the contour level used for λ_{ci}^2. The difference in using the center of the vorticity contours versus using the center of the region identified by λ_{ci}^2 contours was in all cases less than 2.5%, so uncertainty bars of 2.5% are included in Fig. 14a.

There is a large range of r/D values measured by previous studies in the 10°–50° range. With the exception of van 't Riet and Smith's (1975) data, the variability is approximately ±10% at any given circumferential position. Derksen et al. (1999) suggests that, "the strong deviation

Fig. 14 a Comparison of tip vortex trajectory for all three Re cases to data from the literature. Both upper and lower tip vortex trajectories are shown where available. **b** Isosurfaces of circumferential vorticity used to visualize the mean tip vortex structure from the three preceding blades for the highest Re ($\sim$137,000)
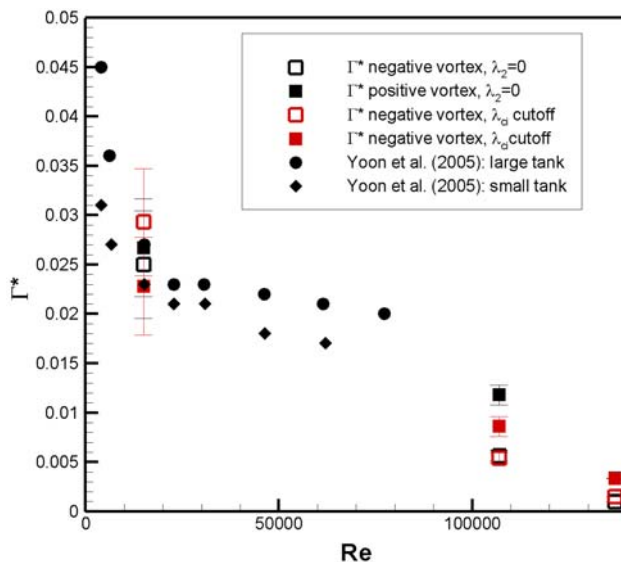
geometrical constraint, but it provides an interesting view on the symmetry of the vortex trajectories; the trajectory from the most recently shed set of tip vortices and measured at 40° and 50° past passage can be reasonably extrapolated to the trajectory of the set of vortices shed two blades prior and measured at 60–100° past passage. The extrapolation breaks down somewhat past 120°, but this is not surprising since the mean tip vortex structure is not expected to be as coherent so far away from the originating blade. In fact, in Yoon et al. (2005), the mean tip vortex structure was noted as coherent only out until about 60° past originating blade passage. A visualization of the capture of the mean tip vortex structure from the three preceding blades for the highest Re ($\sim$137,000) is shown in terms of isosurfaces of circumferential vorticity in Fig. 14b.

Due primarily to the tediousness of the experiments using LDV or standard PIV, previous experimental studies have been quite limited and have rarely considered multiple Re cases. If multiple Re were considered, data were available at only one radius (e.g. Yoon et al. 2005), with the exception of van't Riet and Smith's (1975) early experiments in which no Re dependence was noted between $Re \sim$ 5,000 and $Re \sim$ 90,000.

In the present experiments, multiple Re are considered and data are available within the entire measurement volume. Yoon et al. (2005) suggests that the tip vortices would remain more circumferential (i.e. tighter in towards the blades) for higher Re numbers. It is worth noting that the Re effects observed in Yoon et al. (2005) were slightly noisy and rather weak. Here, a more circumferential structure is seen at the highest Re number (137,000), as remnants of a portion of the vortex shed two blades prior are detected in our measurement volume (Fig. 14b). However, it is also the highest Re case that occupies the middle position in terms of trajectory when compared with the two lower Re cases (Fig. 14a).

If indeed, the trajectory should be most circumferential for highest Re cases, then the presently-measured $Re \sim$ 15,000 trajectory is expected to be at the highest radial position. Whether the fact that it is not is due to an error in experimental measurement, or is a real effect, is not clear. All of the measurements were performed on the same day, in sequence, and both the measurement volume and the instrumentation position remained constant between runs. The angular position of the blades during laser firing has been checked; there is less than 1° of variation between all three Re cases.

The last quantitative measure considered is that of non-dimensional tip vortex strength, Γ^*. The measurement of non-dimensional strength is made in the 40° past blade passage slice, since the previous ones (0°–30°) do not contain the vortex shed off the most recently passed blade.

between [van't Riet's] curve and the other curves is commonly attributed to inertia of the relatively large particles (needed for a photographic technique)". No clear Re dependence is demonstrated in the previous literature. Variability in the data in the literature is often attributed to minor differences in blade or tank geometries; even the thickness of the disk to which the blades are mounted can have a distinct effect on tip vortex structure.

One of the primary differences seen when comparing the present data to previous data is that the range of circumferential positions begins at 40° and continues well past 60° (aligned with the next blade). This is a purely

Fig. 15 Measured magnitude of circulation for positive and negative tip vortices in present experiment (*filled* and *solid squares*), calculated using two different measures of the extent of the vortex core, and data adapted from Yoon et al. (2005) (*smaller, dark symbols*)

The boundary of the vortex is taken to be the line along which $\lambda_2 = 0$ or $\lambda_{ci}^2 = C$ where C is either 0.14, 0.28, or 0.56 depending on which arbitrary measure gives the most similar region to $\lambda_2 = 0$. (Both the $\lambda_2 = 0$ and $\lambda_{ci}^2 = C$ boundaries appear to be a reasonable representation of vortex boundary for the most recently shed vortices.) The strength is calculated numerically by integrating the non-dimensional vorticity.

The uncertainty bars shown in Fig. 15 reflect the fact that there is a portion of the vortex that does not appear in the 40° frame, moreso for the $Re \sim 15,000$ case. Since one would expect the positive and negative vortices to have similar levels of circulation due to symmetry, and ideally for the method of identifying the vortex core to not affect the measurement, a full measure of uncertainty would also account for the variations caused by method of identification and is estimated to be as high as 30% in the present case. Here more emphasis is placed on the trend. Even so, the measurements of Γ^* are reasonably consistent with those given in Yoon et al. (2005). The main difference is that Yoon et al.'s (2005) data appear to suggest that Re independence is reached at a Re above 100,000. No leveling off of Γ^* is yet noted in the present experiments (up to a Re of approximately 137,000).

4 Conclusions

The present measurements are the first instantaneous volumetric measurements of the three-dimensional flow inside a stirred tank reactor. The three-dimensional three-component velocimetry (V3V) method greatly simplifies the process of acquiring this dense dataset by integrating three fixed camera apertures into a single head. Thus, acquisition of data requires only a simple in-situ calibration, and no complex alignment of cameras or Scheimpflug lens mounts, as is commonly the case in stereoscopic measurements. Data for multiple conditions (i.e. multiple Re) are more readily attainable; here, data are acquired and results of tip vortex characterization presented for three Re (15,000, 107,000 and 137,000). The V3V returned approximately 15,000 instantaneous three-dimensional velocity vectors per realization in a cubic volume roughly 12 cm × 12 cm × 10 cm. The irregularly spaced vectors are easily re-interpolated onto a regular grid to facilitate ensemble averaging and the computation of gradient-based quantities.

The data obtained in the present experiments greatly increase the understanding of the complex flow in stirred tanks. Previous single-camera PIV and stereoscopic PIV studies have provided 'glimpses' of the flow features such as the tip vortices and the radial jet and in some cases have provided highly-resolved data in a particular region. With the present method, a better understanding of these features is now available. Isosurfaces of quantities such as velocity, vorticity and turbulent kinetic energy help to visualize the structure of the flow and to identify regions of high mixing potential.

Various methods of tip vortex identification and characterization are compared, including arbitrary cut-offs of normalized vorticity, identification of pressure minima and associated vortex cores based on an eigenvalue criterion for the pressure tensor ($\lambda_2 < 0$), calculation of swirl strength again based on an eigenvalue criterion but associated with the velocity gradient matrix (λ_{ci}^2), and calculation of the principal strain rates (S_{11}^*, S_{22}^*, S_{33}^*) as measures of stretching and compression.

For the first time, PIV data are obtained that give a clear visual picture of the tip vortices well beyond blade passage (up to approximately 140° for the highest Re). The effectiveness of exclusively using an eigenvalue constraint (λ_2, λ_{ci}^2) boundary for identification of tip vortex boundary becomes somewhat limited for positions $\theta > 60°$, as the coherence of the tip vortex as represented in the mean velocity field drops off. When a combination of the two methods of tip vortex identification are used in conjunction with the present data, it is possible to see the tip vortex shed even two blades prior ($\theta > 120°$), at least for a Re of 137,000. (Not being able to view tip vortices for $\theta > 120°$ at the two smaller Re may be due only to geometrical constraints of data acquisition volume).

Further, the $\lambda_2 < 0$ criterion leads to considerably more regions known to be outside of the tip vortex cores being identified as vortical regions, due either to other residual vorticity in the system or noise in the measurement and/or

calculation. The use of an arbitrary cutoff for λ_{ci}^2 as a method of vortex identification more effectively delineates the tip vortex region from other regions of the flow. And while there is a significant difference in identified vortex regions using two-dimensional or three-dimensional data when using the $\lambda_2 < 0$ criterion, there is little difference observed when using a λ_{ci}^2 cutoff suggesting that the λ_{ci}^2 cutoff is preferable both in general for tip vortex identification and when more limited (e.g. two-dimensional) data are all that are available. Principal strain rates are calculated and the general trends compared reasonably to those in Bouremel et al. (2009b).

The tip vortex trajectory for the three Re cases is compared to data in the literature. The tip vortex trajectories appear reasonable when compared to others; however, even with the unique availability of volumetric data from three Re for exactly the same (otherwise) experimental conditions, it is not possible to decisively draw a conclusion on the impact of Re on tip vortex trajectory. Tip vortex circulation compares reasonably to previous measurements available in the literature, although the present data do not suggest Re independence for Re at or below 137,000.

Clearly, the ability to rapidly acquire three-dimensional velocity data in a three-dimensional volume gives a significant advantage for certain types of investigations. There are limitations in terms of the applications; the most significant limitation is perhaps the pre-defined measurement volume. But depending upon the defined research question, the advantages may be worth the cost in resolution or in scaling a test apparatus. In the present case, the ability to efficiently acquire and manipulate these three-dimensional data at three Re, by interactively rotating the impeller-data volume system, making animations of moving slices, etc., has allowed for one of the most detailed studies of a complex mixing flow to date. The data will be made available upon request.

References

Adrian R (1991) Particle imaging techniques for experimental fluid mechanics. Annu Rev Fluid Mech 23:261–304

Adrian RJ (2005) Twenty years of particle image velocimetry. Exp Fluids 39(2):159–169

Arroyo MP, Greated CA (1991) Stereoscopic particle image velocimetry. Meas Sci Technol 2(12):1181–1186

Bouremel Y, Yianneskis M, Ducci A (2009a) On the utilisation of vorticity and strain dynamics for improved analysis of stirred processes. Chem Eng Res Design 87:377–385

Bouremel Y, Yianneskis M, Ducci A (2009b) Three-dimensional deformation dynamics of trailing vortex structures in a stirred vessel. Ind Eng Chem Res. doi:10.102/ie801481v

Burgmann S, Dannemann J, Schroder W (2008) Time-resolved and volumetric PIV measurements of a transitional separation bubble on an SD7003 airfoil. Exp Fluids 44(4):609–622

Chakraborty P, Balachandar S, Adrian RJ (2005) On the relationships between local vortex identification schemes. J Fluid Mech 535:189–214

Derksen JJ, Doelman MS, Van den Akker HEA (1999) Three-dimensional LDA measurements in the impeller region of a turbulently stirred tank. Exp Fluids 27(6):522–532

Ducci A, Yianneskis M (2007a) Vortex identification methodology for feed insertion guidance in fluid mixing. Chem Engr Res Des 85(A5):543–50

Ducci A, Yianneskis M (2007b) Vortex tracking and mixing enhancement in stirred processes. AIChE J 53(2):305–315

Elsinga GE, Scarano F, Wieneke B, Van Oudheusden BW (2006) Tomographic particle image velocimetry. Exp Fluids 41(6):933–947

Escudié R, Liné A (2007) A simplified procedure to identify trailing vortices generated by a Rushton turbine. AIChE J 53(2):523–526

Escudié R, Bouyer D, Liné A (2004) Characterization of trailing vortices generated by a Rushton turbine. AIChE J 50(1):75–86

Hill DF, Sharp KV, Adrian RJ (2000) Stereoscopic particle image velocimetry measurements of the flow around a Rushton turbine. Exp Fluids 29(5):478–485

Hori T, Sakakibara J (2004) High-speed scanning stereoscopic PIV for 3d vorticity measurement in liquids. Meas Sci Technol 15(6):1067–1078

Jeong J, Hussain F (1995) On the identification of a vortex. J Fluid Mech 285:69–94

Kähler C, Kompenhans J (2000) Fundamentals of multiple plane stereo particle image velocimetry. Exp Fluids 29:S70–S77

Lee KC, Yianneskis M (1998) Turbulence properties of the impeller stream of a Rushton turbine. AIChE J 44(1):13–24

Maas H, Gruen A, Papntoniou D (1993) Particle tracking velocimetry in three-dimensional flows. Exp Fluids 5:133–146

Meng H, Pan G, Pu Y, Woodward SH (2004) Holographic particle image velocimetry: from film to digital recording. Meas Sci Technol 15(4):673–685

Ohmi K, Li HY (2000) Particle-tracking velocimetry with new algorithms. Meas Sci Technol 11(6):603–616

Pereira F, Gharib M, Dabiri D, Modarress D (2000) Defocusing digital particle image velocimetry: a 3-component 2-dimensional DPIV measurement technique. Application to bubble flows. Exp Fluids Suppl:S78–S84

Pereira F, Stuer H, Graff EC, Gharib M (2006) Two-frame 3d particle tracking. Meas Sci Tech 17(7):1680–1692

Prasad AK (2000) Stereoscopic particle image velocimetry. Exp Fluids 29(2):103–16

Ranade VV, Perrard M, Xuereb C, Le Sauze N, Bertrand J (2001) Influence of gas flow rate on the structure of trailing vortices of a Rushton turbine: PIV measurements and CFD simulations. Chem Engr Res Des 79(8):957–964

Saarenrinne P, Piirto M (2000) Turbulent kinetic energy dissipation rate estimation from PIV velocity vector fields. Exp Fluids Suppl:S300–S307

Schäfer M, Yu J, Genenger B, Durst F, Akker HEAvd, Derksen JJ (2000) Turbulence generation by different types of impellers. In: 10th European conference on mixing, Elsevier Science, Amsterdam, pp 9–16

Schroder A, Geisler R, Elsinga GE, Scarano F, Dierksheide U (2008) Investigation of a turbulent spot and a tripped turbulent boundary layer flow using time-resolved tomographic PIV. Exp Fluids 44(2):305–316

Sharp KV, Adrian RJ (2001) PIV study of small-scale flow structure around a Rushton turbine. AIChE J 47(4):766–778

Soloff SM, Adrian RJ, Liu ZC (1997) Distortion compensation for generalized stereoscopic particle image velocimetry. Meas Sci Technol 8(12):1441–1454

Stoots CM, Calabrese RV (1995) Mean velocity field relative to a Rushton turbine blade. AIChE J 41(1):1–11

van't Riet K, Smith J (1973) The behaviour of gas-liquid mixtures near Rushton turbine blades. Chem Eng Sci 28:1031–1037

van't Riet K, Smith JM (1975) Trailing vortex system produced by Rushton turbine agitators. Chem Eng Sci 30(9):1093–1105

van't Riet K, Bruijn W, Smith J (1976) Real and pseudo-turbulent in the discharge stream from a Rushton turbine. Chem Eng Sci 31(6):407–412

Virant M, Dracos T (1997) 3d PTV and its application on Lagrangian motion. Meas Sci Technol 8(12):1539–1552

Wernet M (2004) Planar particle imaging Doppler velocimetry: a hybrid PIV/DGV technique for three-component velocity measurements. Meas Sci Technol 15:2011–2028

Willert C, Gharib M (1992) Three-dimensional particle imaging with a single camera. Exp Fluids 12:353–358

Willert C, Hassa C, Stockhausen G, Jarius M, Voges M, Klinner J (2006) Combined PIV and DGV applied to a pressurized gas turbine combustion facility. Meas Sci Technol 17(7):1670–1679

Yianneskis M, Popiolek Z, Whitelaw JH (1987) An experimental study of the steady and unsteady flow characteristics of stirred reactors. J Fluid Mech 175:537–55

Yoon HS, Hill DF, Balachandar S, Adrian RJ, Ha MY (2005) Reynolds number scaling of flow in a Rushton turbine stirred tank. Part I—mean flow, circular jet and tip vortex scaling. Chem Eng Sci 60(12):3169–3183

Zhou J, Adrian RJ, Balachandar S, Kendall TM (1999) Mechanisms for generating coherent packets of hairpin vortices in channel flow. J Fluid Mech 387:353–396